5864 *Biochemistry* **2009,** *48,* 5864–5873
DOI: 10.1021/bi900493n

BIOCHEMISTRY
including biophysical chemistry & molecular biology
Article

Membrane Attachment Facilitates Ligand Access to the Active Site in Monoamine Oxidase A[†]

Rossen Apostolov,[‡] Yasushige Yonezawa,[‡] Daron M. Standley,[‡] Gota Kikugawa,[§] Yu Takano,[‡] and Haruki Nakamura*[,‡]

[‡]*Institute for Protein Research, Osaka University, 3-2 Yamadaoka, Suita, Osaka 565-0871, Japan, and* [§]*Institute of Fluid Science, Tohoku University, 2-1-1 Katahira-Aobaku, Sendai, Miyagi 980-8577, Japan*

Received March 23, 2009; Revised Manuscript Received May 15, 2009

ABSTRACT: Monoamine oxidase membrane enzymes are responsible for the catalytic breakdown of extra- and intracellular neurotransmitters and are targets for the development of central nervous system drugs. We analyzed the dynamics of rat MAOA by performing multiple independent molecular dynamics simulations of membrane-bound and membrane-free forms to clarify the relationship between the mechanics of the enzyme and its function, with particular emphasis on the significance of membrane attachment. Principal component analysis of the simulation trajectories as well as correlations in the fluctuations of the residues pointed to the existence of three domains that define the global dynamics of the protein. Interdomain anticorrelated movements in the membrane-bound system facilitated the relaxation of interactions between residues surrounding the substrate cavity and induced conformational changes which expanded the active site cavity and opened putative pathways for substrate uptake and product release. Such events were less pronounced in the membrane-free system due to differences in the nature of the dominant modes of motion. The presence of the lipid environment is suggested to assist in decoupling the interdomain motions, consistent with the observed reduction in enzyme activity under membrane-free conditions. Our results are also in accordance with mutational analysis which shows that modifications of interdomain hinge residues decrease the activity of rat MAOA in solution.

Monoamine oxidase (MAO)[1] enzymes catalyze the oxidative deamination of various biogenic monoamines (*1*, *2*). They break down neurotransmitters such as serotonin and dopamine in the synaptic cleft and thus regulate the function of the central nervous system. Enzyme malfunction leads to various psychological disorders such as aggressive behavior, criminality, social phobias, depression, and substance abuse, which has made these proteins one of the major targets for antidepressant drugs (*3*, *4*). MAO inhibitors have also been successfully used for suppressing the production of neurotoxins like MPP+ (*5*, *6*), an agent directly linked to the development of Parkinson's disease. Moreover, they have found application in the treatment of oxidative stress conditions (*7*, *8*) because one of the products of the amine oxidation is hydrogen peroxide, a very powerful source of hydroxyl radicals. Clinical trials have given hope for their possible use as agents against Alzheimer's disease (*9*), Huntington's disease (*10*), and amyotrophic lateral sclerosis (*11*). The spectrum of serious diseases that can possibly be treated by controlling MAO function has stimulated extensive research, including mutagenesis studies (*2*) and docking simulations (*12*−*15*) in the hope of improving our understanding of their structure−function relationship and kinetics.

MAOs comprise two isoenzymes, MAOA and MAOB, which exhibit different substrate sensitivities due to differences in the size, shape, and chemical environment of the active site pockets (*16*). MAOA is also the first membrane protein discovered to form a single transmembrane helix, clearly seen in the crystal structure of rat MAOA (*17*). Experiments have suggested that membrane incorporation is important for protein function since, under membrane-free conditions, rat MAOA (*18*) and human MAOA (*19*) activities drop approximately 4 times, while truncation of the transmembrane helix of human MAOB decreases its activity by a factor of 10 (*20*). Many of the MAO structures are resolved at very high resolution and provide detailed information about the active site, which is needed for successful design of new inhibitors. Unfortunately, due to difficulties in obtaining non-coagulating apo forms, all of the deposited structures contain various bound inhibitors. The substrate binding regions are found deep in the interior of the extracellular domain unit, and

[†]We are grateful to the Ministry of Education, Culture, Sports, Science and Technology (MEXT) of Japan for a Grant-in Aid for Scientific Research on Priority Area "Structures of Biological Macromolecular Assemblies" (513-18054013 and 513-20051013).

*To whom correspondence should be addressed. E-mail: harukin@protein.osaka-u.ac.jp. Telephone: +81 (0)6 6879 4311. Fax: +81 (6) 6879 8636.

[1]Abbreviations: MAO, monoamine oxidase; MD, molecular dynamics; PCA, principal component analysis; ENM, elastic network model; POPC, 1-palmitoyl-2-oleoyl-*sn*-glycero-3-phosphocholine; FAD, flavine adenine dinucleotide; rmsd, root-mean-square deviation; TM, transmembrane.

 Published on Web 05/20/2009

there is no easily identifiable route for substrate access to the active site. The lack of inhibitor-free crystal structures makes it difficult to infer the conformational changes that define the function of the enzyme. These changes may include collective displacements of domains to facilitate access to the catalytic region for substrate attack. It is possible to identify such domains and the direction of their displacements using several computational methods.

In this work, we analyzed the dynamics of rat MAOA using molecular dynamics (MD) simulations (*21*) of the full-length protein embedded in a 1-palmitoyl-2-oleoyl-*sn*-glycero-3-phosphocholine (POPC) lipid bilayer and of the membrane-unbound system by truncating the extracellular unit in solvent, with principal component analysis (PCA) of the trajectories. Rat MAOA was chosen because, at the time, the crystal structure [Protein Data Bank (PDB) entry 1o5w] was the only member of the MAO family that had a resolved transmembrane helix (TMH). The length of the TMH is essential in investigating how the protein dynamics is affected by membrane insertion. Moreover, the C_α rmsd between 1o5w and a more recently determined structure (PDB entry 2z5x) is less than 0.7 Å. Thus, although the resolution of 1o5w (3.2 Å) is not as good as that of 2z5x (2.2 Å), we are sure that our statistical analyses based on time averages of structural ensembles derived from MD simulations are sufficient.

The results from the PCA analysis, along with elastic network model (ENM) analysis (*22*, *23*), suggested the existence of three dynamical domains within the extracellular unit. The dynamics of these domains differed significantly, depending on whether the protein was embedded in the membrane, suggesting that membrane anchoring might have a direct role in enhancing enzyme function.

METHODS

The initial structure of the rat MAOA monomer was obtained from the Protein Data Bank [entry 1o5w (*17*)]. The crystal structure does not include the first nine N-terminal and last six C-terminal residues; therefore, they were excluded from the model. Instead, acetyl and *N*-methylamine residues were used to cap the termini. Missing hydrogen atoms were added using the tplgene module of the myPresto simulation suite (*24*). The flavine adenine dinucleotide (FAD) cofactor was added to the simulation system after structure optimization and electrostatic potential (ESP) charge calculation using Gaussian (*25*) with the 6-31G* basis set. No inhibitor or substrate was included in the model. Rat MAOA forms a homodimer in the crystal structure. However, other homologues, such as human MAOA, are found to crystallize and retain catalytic activity in vitro as monomers (*16*), while bovine MAOB is shown to exist and function as a tetramer or larger oligomeric complex (*26*). To the best of our knowledge, there is no evidence showing that dimerization is required for rat MAOA to function. Therefore, we performed all simulations on the monomer. Atomic interactions were modeled according to the CHARMm22 force field (*27*). Polar hydrogen bonds, including water molecules, were treated as rigid bodies which allowed for a 2 fs time step. Rigid body treatment was based on integration of the Euler equations of motion of a rigid body, as described in ref (*28*). Electrostatic interactions were calculated using the smooth particle-mesh Ewald method (*29*) with a grid size of 1 Å per cell. A cutoff distance of 12 Å was used for the Ewald real space and van der Waals truncation. The Ewald convergence parameter α was set to 0.35 $Å^{-1}$. All calculations were conducted with the cosgene MD engine of myPresto (*24*) on three hardware platforms: SGI Altix 4000 server, Intel Xeon 3.2 GHz cluster, and MDGRAPE-3 special purpose accelerator board (*30*). The membrane-bound system was modeled by embedding the monomer in a pre-equilibrated POPC lipid bilayer of 163 chains. Two opposing POPC chains, one from each leaflet of the bilayer, were removed, and the TM helix of MAOA was inserted into the cavity. The whole system was then solvated in 17125 water molecules. In addition, 76 sodium and 78 chloride ions were added to neutralize the total charge and bring the tonicity of the solvent to physiological levels of 0.9%. The complete system consisted of 81647 atoms. The size of the rectangular cell was 72 Å × 94 Å × 124 Å. The energy of the system was locally optimized using 3000 steps of conjugated gradient minimization. This was followed by a 100 ps equilibration of the membrane chains and the solution under NPT (constant pressure and constant temperature) conditions, while keeping the positions of the protein and the cofactor atoms fixed. The constraints were then slowly relaxed for an additional 100 ps. Production runs were conducted without any constraints using an NPT ensemble. Temperature and pressure were controlled by coupling the system to a Nose-Anderson barostat and thermostat with coupling times of 2 and 0.1 ps, respectively, for achieving constant conditions of 1 bar and 310 K. A snapshot 2 ns from the trajectory, when the root-mean-square deviation (rmsd) of the C_α atom fluctuations had reached a plateau, was used as a base for the construction of the membrane-unbound system. Residues from Leu501 to Ile521 that form the transmembrane (TM) helix were removed and substituted with an *N*-methylamine cap. Lipids were also removed and replaced with water. The new system had dimensions of 72 Å × 92 Å × 96 Å with 63605 atoms. Energy minimization and equilibration were performed in the same way as in the membrane-bound system. We performed three independent, 20 ns long production runs for each of the systems for a total of 120 ns of trajectory data. For each run, we used a different random distribution of initial velocities. Trajectory snapshots were taken every 2 ps for subsequent analysis.

Conformational changes of the protein during the six simulation trajectories were monitored by calculating the rmsd of the C_α atoms after aligning them to the initial minimized structure using the standard method for mass-weighted least-squares fitting. The degree of collective motions between different groups of atoms was assessed from the cross-correlation matrix with elements

$$\mathrm{Corr}_{ij} = \langle(\vec{r_i} - \langle\vec{r_i}\rangle)\cdot(\vec{r_j} - \langle\vec{r_j}\rangle)\rangle / \sqrt{\langle(\vec{r_i} - \langle\vec{r_i}\rangle)^2\rangle\langle(\vec{r_j} - \langle\vec{r_j}\rangle)^2\rangle}$$

Each element represents the correlation of the movements of atoms *i* and *j*. In the case of fully linearly correlated movements, Corr_{ij} equals 1, while in the case of anticorrelated motions it is −1 and in the case of noncorrelated or perpendicular motions 0. The simulation trajectories were analyzed for dominant collective displacements using PCA of the fluctuations of C_α atoms (*31*, *32*). The average structure of each trajectory was projected along chosen high-eigenvalue modes. The two extreme projections were then used for dynamical domain analysis using DynDom (*33*).

Structural domains in the static crystal structure were assigned using Protein Domain Parser (PDP) (*34*). The search for putative

routes leading to the active site was done using Caver (*35*), which provides the direction, size, and identity of atoms defining the tunnel walls. Each structure was searched for multiple tunnels sorted by the size of the narrowest part of the tunnel. Water, lipid, and ions were removed from the trajectory snapshots, and the search was performed for six tunnels starting at 4 Å from the riboflavin reactive site of FAD. The ENM method was implemented in the *myPresto* program suite following the algorithm in the ElNemo (*22*) server. We used only the C_α atoms of each residue of the crystal structure and let them interact with other residues within a 9 Å cutoff via a spring potential (*23*). They were assigned the same mass, 12.01 amu.

Figures of the MAOA structure were prepared using VMD (*36*). Sequence alignment was done using clustalw (*37*) and seaview (*38*). Graphs were prepared using gnuplot (*39*), and the manuscript was prepared with Lyx (*40*) and Jabref (*41*).

RESULTS AND DISCUSSION

Overview of MAOA Topology. Most of the mass of MAOA is concentrated into a compact extracellular structure, which is attached at its C-terminus to the membrane through a single 21-residue transmembrane α-helix. The FAD cofactor and the active site are buried deep in the interior of the protein. The structure can be functionally divided into two domains, the FAD-binding domain (domain F, residues 10−50, 227−287, and 427−473) and the substrate binding domain (*17*). Analysis of MD simulation data as well as analysis of the crystal structure using PDP suggests that the substrate binding domain is actually composed of two subdomains. We will refer to these as membrane binding domain M (residues 112−208, 288−300, and 408−426) and substrate binding domain S (residues 51−111, 209−226, 301−407, and 474−486). As indicated by the residue ranges given above, the domains consist of noncontinuous segments, implying a tight coupling between them. The domains share a large amount of surface area, and their separation is not obvious from the static structure. Domain M is thought to be partially embedded in the membrane (*17*), as confirmed by MD simulations of the highly homologous MAOB (*42*). In Figure 1a, a schematic view of the major structural elements is shown. A snapshot at 5 ns from the membrane-bound system trajectory is shown in Figure 1b. Disordered outer loop L, transmembrane helix TM, and the active site pocket are also shown with the corresponding crystal structure (Figures 1c,d).

Residues lining the active site cavity were defined as those for which at least one atom could be found within 6 Å of the inhibitor in the crystal structure. These residues form two walls that are part of domains M and S. The first wall comprises residues entirely from substrate binding domain S: 97, 108, 305, 323−325, 335−337, 350, and 352. The second wall is constructed by residues mainly from membrane binding domain M: 66−69, 197, 207−210, 215, 406, and 444. Residues 110, 111, and 180−182 are positioned between the two walls, on opposite sides of the active site cavity.

Dynamics and Stability of the Membrane-Bound and Membrane-Unbound Enzymes. After <5 ns, the average C_α rmsd of the membrane-bound MAOA in the three separate runs reached ~3 Å and retained this value throughout the simulation. A major contribution to this rmsd came from the first four N-terminal residues, outer loop L, and helix TM, as the cytoplasmic domains slightly tilted and relaxed toward the membrane plane. When we excluded these residues and considered

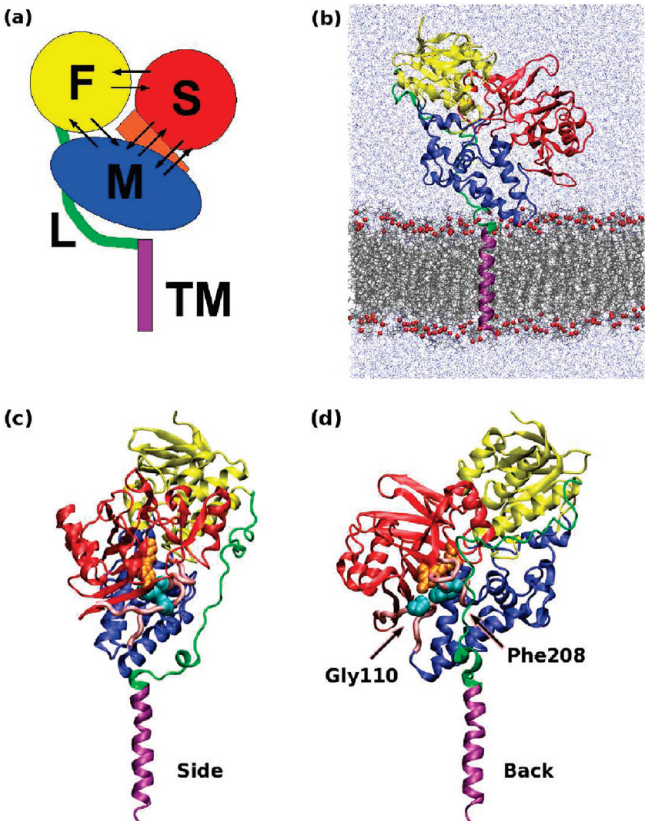

FIGURE 1: (a) Schematic view of the topology of MAOA showing FAD cofactor binding domain F (yellow), substrate binding domain S (red), membrane binding domain M (blue), surface loop L (green), and transmembrane helix TM (purple). The active site, situated between domains S and M, is depicted as an orange rectangle. (b) A snapshot at 5 ns from the membrane-bound system. (c and d) Crystal structure of MAOA in cartoon representation. Domain colors in panels b−d are the same as in panel a. Inhibitor clorgyline is shown in an orange space-filling representation. Loops 105−115 and 205−215 are shown as pink tubes, and conserved residues Gly110 and Phe208 are shown in a cyan space-filling representation.

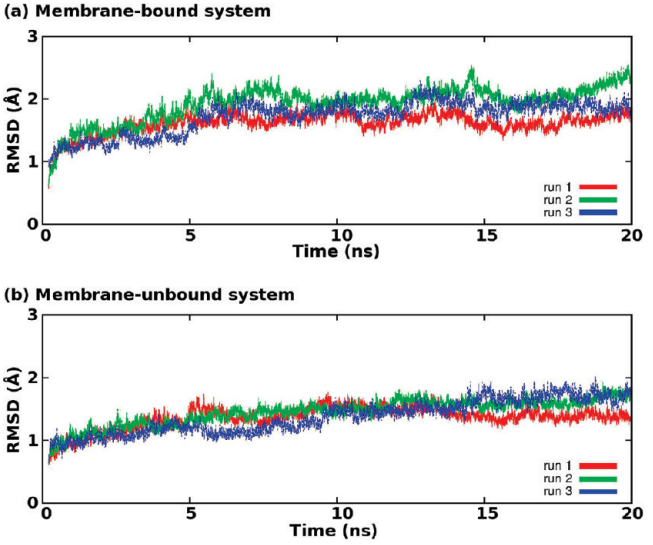

FIGURE 2: Time dependence of the rmsd calculated using all C_α atoms from the M, F, and S domains from each of the three runs in the (a) membrane-bound system and (b) membrane-unbound system.

only residues from position 14 to 464, i.e., the M+S+F superdomain, the average rmsd of the three runs reached a plateau of

only ~1.9 Å after 6 ns (Figure 2a). Throughout the simulation run, domain M remained partially embedded, supported by electrostatic interactions between the phospholipid groups and a ring of positively charged residues (Lys102, Arg129, Lys163, Lys168, and Arg171). Outer loop L was very flexible and remained disordered. A short α-helix from residue 355 to 375, positioned on the surface of the S domain, also exhibited high mobility.

In a fashion similar to that of the membrane-bound system, the rmsd of the membrane-unbound MAOA chains in the three runs rose sharply over the first 2 ns to an average of ~1.7 Å and then slowly increased until reaching a ~2.2 Å plateau after 10 ns.

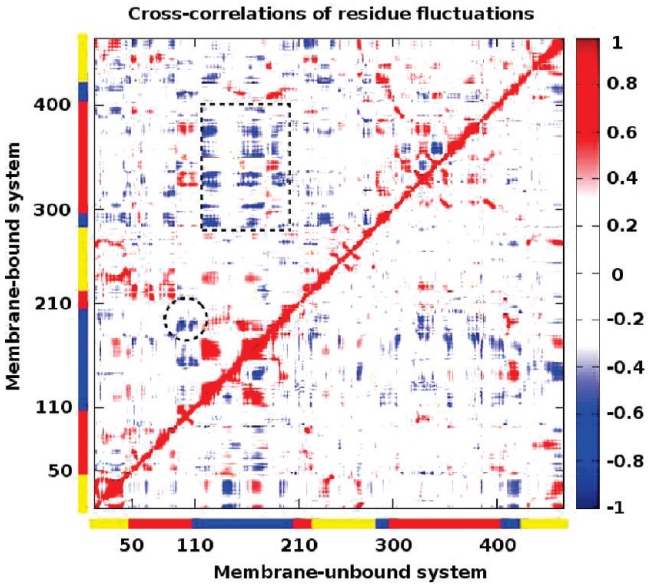

FIGURE 3: Cross-correlation coefficients for the membrane-bound system (top left triangle) and the membrane-unbound system (bottom right triangle). The correlation matrix was constructed using the last 10 ns of each of the simulated trajectories; i.e., a total of 30 ns per system were used for the statistical analysis. The positions of the different domains from Figure 1 are shown as colored bars at the bottom and left sides of the map. In the membrane-bound system, domain M (residues 110−210) shows more pronounced anticorrelated motion relative to the other two domains, as indicated by the dotted line rectangle. Anticorrelation in the movements of loops from residue 105 to 115 and from residue 205 to 215 is also more pronounced in the membrane-bound system (dotted circle).

Outer loop L was much more flexible than in the membrane-bound system, where it was partially stabilized by membrane interactions. Excluding the loop from the fit, we could see that the system was equilibrated at 10 ns, with an average rmsd of 1.5 Å as shown in Figure 2b. The lack of membrane environment allowed the C-terminus of the outer loop to adopt various conformations and repeatedly change the nature of interactions with the edge of domain M, residues 116−126.

Global correlated motions among residues could be observed by examining the cross-correlation matrix of inter-residue fluctuations, as shown in Figure 3. The correlation matrix was constructed using the last 10 ns of each of the simulated trajectories; i.e., a total of 30 ns per system were used for the statistical analysis. Domains M, S, and F could be identified by examining the red squares along the diagonal with off-diagonal red areas indicating their interconnections. In both systems, the domains are clearly defined by the symmetry of the squares and the corresponding off-diagonal elements. We monitored the changes in the range of the segment definitions during the simulation runs to account for possible major conformational rearrangements. We analyzed structures taken at 10 and 20 ns from all six trajectories. As one can see from Table 1 and Figure 4, the overall three-part domain decomposition pattern found in the crystal structure is preserved in all snapshots.

Considering interdomain motions, some important differences could be observed that might be biologically relevant. There was a more pronounced anticorrelation in the motions of domain M relative to domains S and F in the membrane-bound system compared to the membrane-unbound one (dotted rectangles in Figure 3). This is a potentially important result since regulation of access to the active site, positioned between domains M and S, should require a decoupling of the domain movements.

In addition, we observed high anticorrelations between the loops formed by residues 105−115 and 205−215 (dotted circle in Figure 3). As seen from the sequence alignment of rat MAOA homologues (Figure 5), the amino acid residues in these two loops are well-conserved. In particular, Gly110 is conserved across the family, while Phe208 is conserved within the A-type isoform and replaced with Ile in the B-type isoform. Mutation of Gly110 with Ala (*18*) produces species which exhibit 11-fold lower activity in solution. Moreover, substrate recognition analysis of mutants with Phe208 replaced with Ile (*43*) has shown

Table 1: Residue Ranges That Define the Segments of Dynamical Domains in the Crystal Structure[a]

method	domain M	domain S	domain F
PDP, crystal structure	112−208, 288−300, 408−426	51−111, 209−226, 301−407, 474−486	10−50, 227−287, 427−473
PDP (MEM) (1), 10 ns	111−204, 485−496	90−110, 205−217, 303−399	10−89, 218−302, 400−484
PDP (MEM) (1), 20 ns	112−208	51−111, 209−226, 301−406	9−50, 227−300, 407−474
PDP (MEM) (2), 10 ns	112−208, 486−505	51−111, 209−226, 299−408	9−50, 227−298, 409−465
PDP (MEM) (2), 20 ns	111−214, 284−302, 400−426, 488−505	92−110, 303−399	9−91, 215−283, 427−472
PDP (MEM) (3), 10 ns	112−208, 488−505	53−111, 209−226, 303−396	9−52, 227−302, 397−472
PDP (MEM) (3), 20 ns	112−208, 256−300, 408−428, 485−505	51−111, 209−226, 301−407	9−50, 227−285, 429−460
PDP (UNB) (1), 10 ns	120−211	98−119, 212−224, 311−407	10−97, 225−310, 408−494
PDP (UNB) (1), 20 ns	111−208, 485−500	53−110, 209−226, 303−396	10−52, 227−302, 397−484
PDP (UNB) (2), 10 ns	111−215, 485−500	11−110, 303−395	10−90, 216−302, 396−484
PDP (UNB) (2), 20 ns	112−208, 484−500	53−111, 209−226, 303−396	227−302, 397−483
PDP (UNB) (3), 10 ns	111−208	53−110, 209−226, 303−399	227−302, 400−474
PDP (UNB) (3), 20 ns	113−203	53−112, 204−226, 303−399	227−302, 400−472
ENM, mode 13	49−52, 67−86, 112−229, 295−304, 327−330, 397−422, 435−450, 476−486	53−66, 87−111, 305−326, 331−396	10−48, 230−294, 423−434, 451−475

[a] At 10 and 20 ns, snapshots from the membrane-bound (MEM) and membrane-unbound (UNB) MD simulations; in the normal mode 13 as derived from ENM analysis.

that this residue is important for the selectivity of ligands in the two isoforms. In addition, the two loops define the boundaries of the largest segment of domain M, separating it from domain S. Also, as we explain in more detail below, a major tunnel leading from the active site to the exterior passes between these two loops. These results suggest the importance of the two loops for enzyme function. The effects of membrane attachment on the global dynamics of the enzyme were further investigated by analyzing the principal modes of motion as obtained from PCA analysis of the trajectory data.

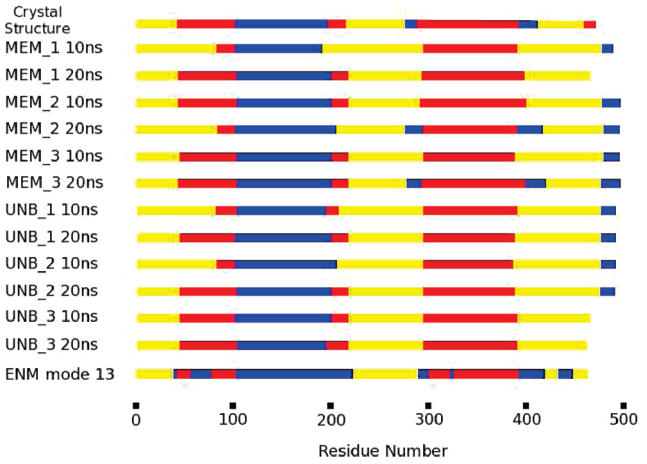

FIGURE 4: Residue ranges that define the segments of dynamical domains in the crystal structure, snapshots at 10 and 20 ns from the MD runs, and in the normal mode 13 from the ENM analysis. Colors are as in Figure 1.

Membrane Attachment Affects Global Dynamics. PCA drastically reduces the high dimensionality of a simulation trajectory to a few orthogonal vectors which account for most of the observed variance in the atomic fluctuations. In this way, the protein dynamics can be understood by examining only the motions along the principal components. When PCA is applied to large molecular systems, special care should be given to distorted regions. Their high-amplitude fluctuations can introduce significant artifacts during the superpositioning procedure and calculation of the variance. Outer loop L, residues 465−500, was one such region on the MAOA surface and was omitted from the analysis, along with the first four N-terminal residues, 10−13. Therefore, in this work, we performed PCA on C_α atoms from residue 14 to 464, i.e., domains M, F, and S. We used the last 10 ns of each of the simulation trajectories, thus analyzing 15000 snapshots per system. Principal components extracted from the membrane-bound system will be termed $PC1_{MEM}$, $PC2_{MEM}$, etc., in order of their decreasing eigenvalues. In the same way, $PC1_{UNB}$, $PC2_{UNB}$, etc., will be used to refer to the membrane-unbound system.

The contribution of every eigenvector to the total observed dynamics was assessed by examining the percentage of its eigenvalue from the total covariance matrix trace. In the case of MAOA, the dynamics of the embedded and membrane-unbound systems appeared to occur mainly along the first principal components, the subspace of which accounted for 40 and 35% of the total variance, respectively.

In the membrane-bound system, the dynamics of the protein were governed by complex twist-type displacements of domain F relative to domain M, and twist- and closure-type motions of domain S relative to domain M along $PC1_{MEM}$ (Figure 6a).

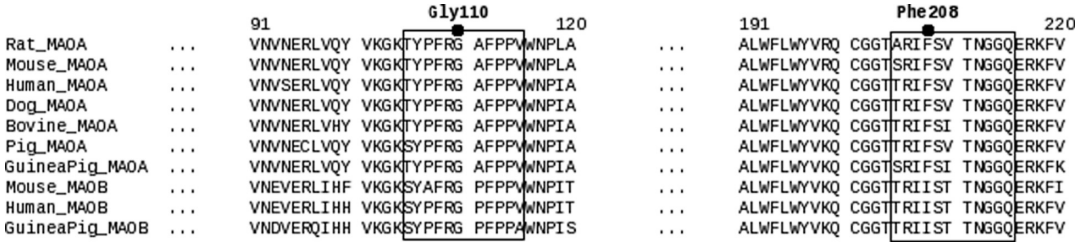

FIGURE 5: Sequence alignment of rat MAOA homologues. Gly110 is conserved across the family. Phe208 is conserved within the A-type isoform and replaced with Ile in the B-type isoform.

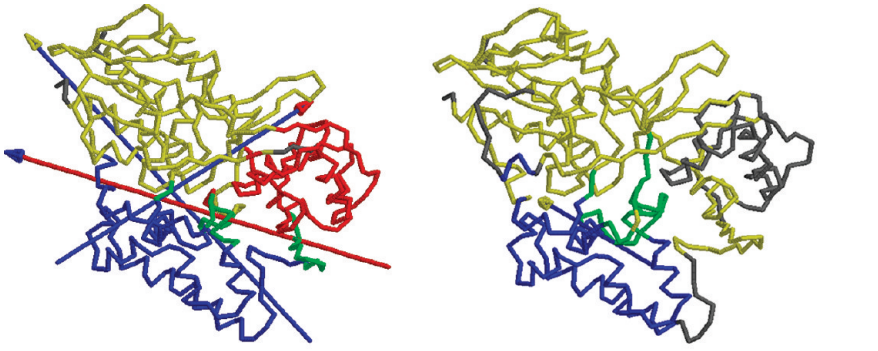

FIGURE 6: Principal components of MAOA dynamics in membrane-bound and membrane-unbound systems and correspondence of the modes. Arrows represent the axes of motion. The colors of the arrow shaft and head correspond to the color of the static and dynamic domains, respectively. Hinge residues are colored green. $PC1_{MEM}$ represents a complex twist motion of F (yellow) relative to M (blue), and two motions of closure and twist of S (red) relative to M. It accounts for 40% of the total variance in the fluctuations. $PC1_{UNB}$ (35% of total variance) represents a twist motion of domain F (yellow) relative to domain M (blue). A large part of domain S (gray) does not participate in a dynamical motion along the principal component.

These motions decoupled domain M from the other two domains, relaxed the interactions between residues lining the active site walls, and were a major source of the observed anticorrelations in the cross-correlation matrix (Figure 3, top left triangle). Dominant motions in the membrane-unbound system defined only two dynamical domains, M and F. Decoupling of the motions of domain M from superdomain S, as seen in $PC1_{MEM}$, could not be found in $PC1_{UNB}$ (Figure 6b).

On the basis of the nature of the dominant modes of conformational changes in the two systems, we propose that the membrane affects the dynamics of the enzyme by immobilizing the membrane-binding domain and thus facilitating a decoupling of its motions from those of the substrate- and FAD-binding domains. This effect is more difficult to achieve under completely solvated conditions because of the compact structure of the enzyme, and the large amount of shared surface area between the domains.

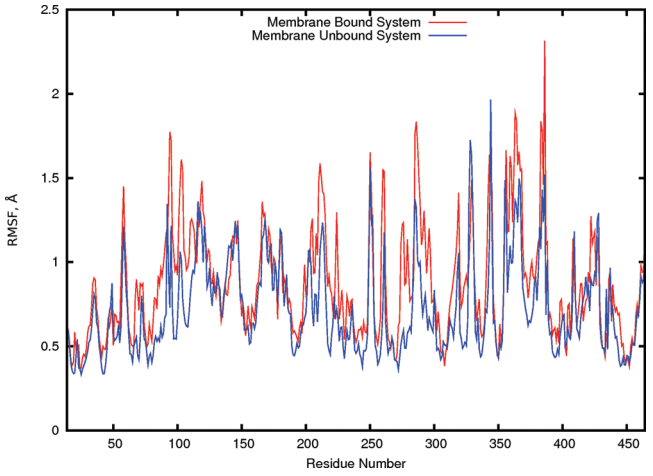

FIGURE 7: Root-mean-square fluctuations of C_α atoms from membrane-bound (red line) and membrane-unbound (blue line) systems. Residues 110−115 and 200−211 exhibit greater displacements in the membrane-bound system.

The dominance of the $PC1_{MEM}$ mode might also be responsible for the highly anticorrelated motions of the two loops, residues 105−115 and 205−215, as seen in the cross-correlation analysis, since these loops form the hinges that connect the dynamical domains of this mode. Also, the atoms of the loops exhibited higher root-mean-square fluctuations (Figure 7) in the membrane-embedded structure than in the membrane-unbound one. These results can be directly linked to the observed opening of one of two tunnels leading to the active site, as discussed below.

Intrinsic Flexibility of the Protein Structure. ENM analysis is a powerful method for extracting the normal modes of a given structure. It has been shown that biologically relevant motions of proteins can be found among a few of the low-frequency modes (*44*, *45*). The topology of the protein structure, rather than the exact form of the interactions between the atoms, has been suggested to be the main factor that determines the nature of the low-frequency spectrum (*46*). ENM is especially useful for analysis of large biomolecules and supramolecular complexes in which complete sampling of their conformational spaces is not feasible by current MD simulation methods. Examination of the low-frequency subspace of normal modes of rat MAOA could guide our understanding of the intrinsic flexibility of the structure and suggest which degrees of freedom might be exploited for functionally relevant conformational changes.

ENM always generates six zero-frequency modes corresponding to rigid-body rotations and translations. As can be seen from Figure 8, the first five non-zero frequency modes, 7−11, exhibit

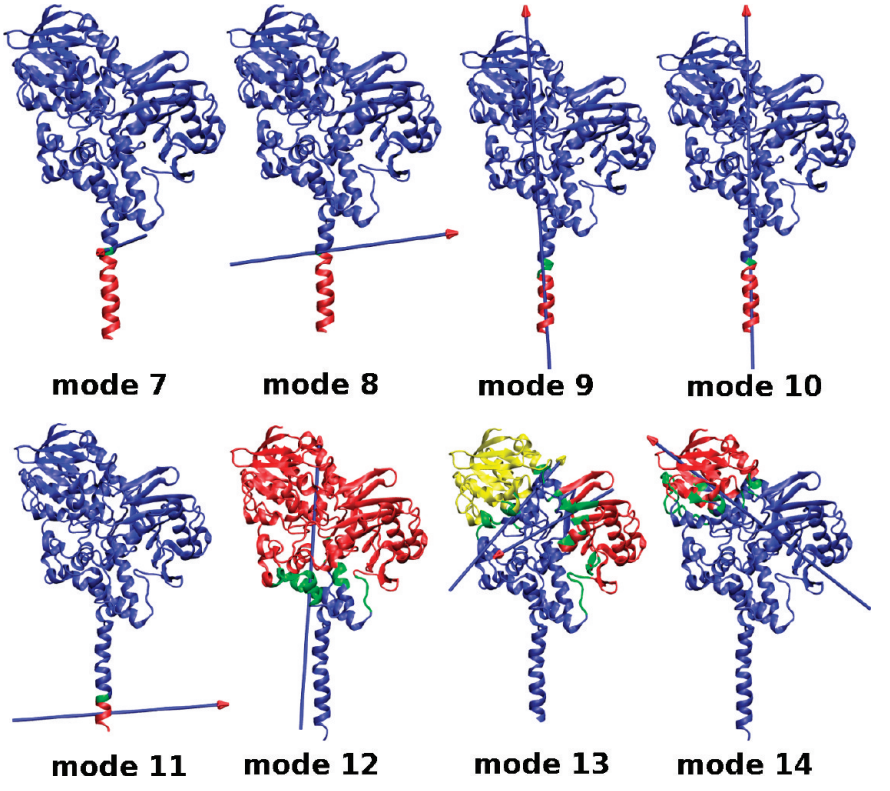

FIGURE 8: Low-frequency normal modes. Modes 7−11 define bendings and twists of the transmembrane helix. Decoupling of interdomain motions within the extracellular unit is first seen in mode 12, while mode 13 defines domain decomposition seen in the first principal component of the membrane-bound system, $PC1_{MEM}$. The arrow colors are the same as in Figure 6.

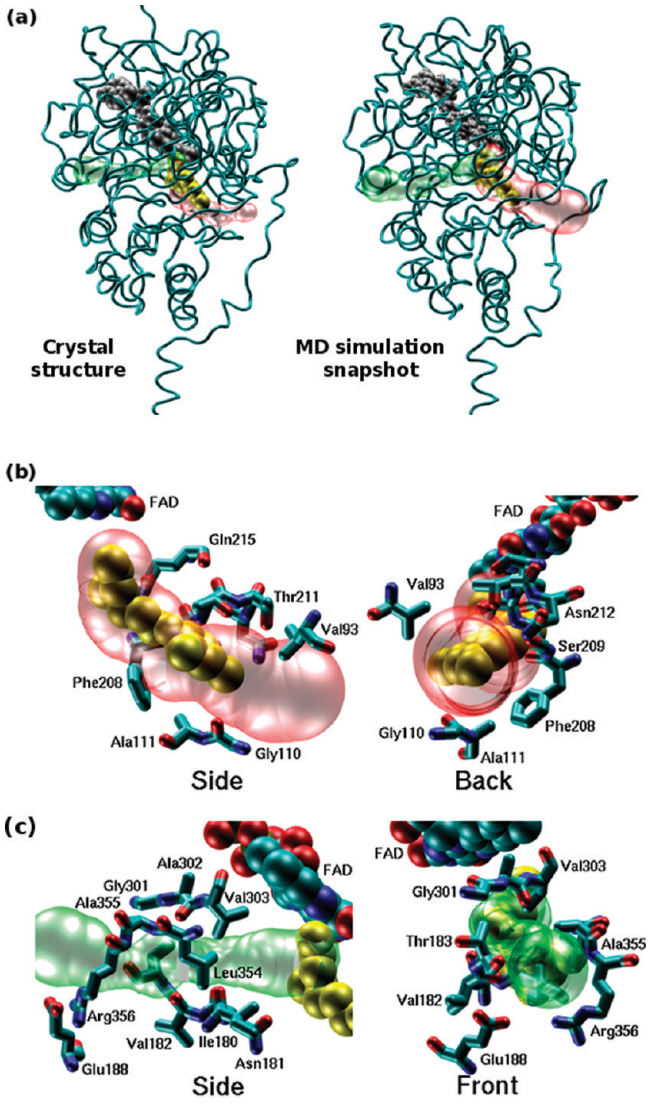

FIGURE 9: (a) Tunnels leading from the active site to the protein exterior. The major tunnel (red), minor tunnel (green), clorgyline inhibitor (yellow), and FAD cofactor (gray) are shown. MAOA is shown in tube representation. The view corresponds to the "side" view in Figure 1c. Close-up view of the (b) major and (c) minor tunnels. The "side" and "back" views are as in Figure 1c,d. Heavy atoms of residues lining the tunnels are shown in licorice representation. Inhibitor clorgyline (yellow) and the FAD cofactor are shown as space-filling spheres.

bending of the transmembrane helix. In these modes, the extracellular domain unit is rigid and static; thus, they are unlikely to be relevant to enzyme function. In the next mode, 12, we could observe a separation of the movement of the membrane-binding domain with the TM helix from the substrate- and FAD-binding domains. The next mode, 13, identifies three dynamical domains within the extracellular unit. The nature of this mode resembles $PC1_{MEM}$ where we saw a similar decoupling of the domain motions. This suggests that during the simulation, degrees of freedom defined by the inherent flexibility of the structure are being explored. The domain ranges are very close to those obtained by applying PDP to the crystal structure and MD trajectory snapshots from the two simulations (Table 1 and Figure 4) and support the suggested domain decomposition. In summary, our MD simulations are consistent with the ENM dynamics with regard to domain definition and their overall motions.

Table 2: Properties of the Tunnel Radii in the Different Simulation Runs for the Membrane-Bound (MEM) and Membrane-Unbound (UNB) Systems

tunnel	average radius (Å)	standard deviation (Å)	maximum radius (Å)
$major_{MEM}$ (1)	1.65	0.28	2.65
$minor_{MEM}$ (1)	1.25	0.14	1.67
$major_{MEM}$ (2)	1.50	0.31	2.58
$minor_{MEM}$ (2)	1.09	0.20	1.74
$major_{MEM}$ (3)	0.95	0.18	1.52
$minor_{MEM}$ (3)	0.89	0.20	1.59
$major_{UNB}$ (1)	1.48	0.20	2.06
$minor_{UNB}$ (1)	1.12	0.18	1.73
$major_{UNB}$ (2)	1.56	0.24	2.20
$minor_{UNB}$ (2)	0.92	0.14	1.51
$major_{UNB}$ (3)	1.24	0.26	1.95
$minor_{UNB}$ (3)	1.00	0.15	1.61

Putative Routes to the Active Site. Several high-resolution crystal structures of MAOB contain water molecules interacting with bound inhibitors in the active site vicinity. The crystal structure of rat MAOA does not show the presence of water in the protein interior, likely due to the lower resolution of the structure. Analysis of the raw MD trajectory data, though, showed the formation of two water-filled tunnels that might grant substrate access (Figure 9). The average, the standard deviation, and the maximum of the tunnel radii in the different runs are listed in Table 2.

The major tunnel passes through the active site cavity and exits through the space formed by residues Val93, Gly110, Ala111, Phe208, Ser209, Val210, Thr211, Asn212, and Gln215 (Figure 9b). In two of the membrane-bound system runs (Figure 10a,b), the size of the tunnel was sufficient for substrate molecules to pass. The tunnels were often open at more than 2.5 Å (Table 2), while the radius of a benzene ring, the widest part of a typical substrate, is approximately 2.25 Å. Two of the tunnel lining residues, Phe208 and Gln215, also define a wall of the cavity and are involved in hydrophobic contacts with the clorgyline inhibitor molecule, as seen in the crystal structure. It should also be noted that Phe208 is conserved within the MAOA family and is replaced with Ile in MAOB. Moreover, cross-mutational analysis of the two isoforms indicated that residue 208 is essential for defining the specificity for different substrates (*43*). Also, it has been proposed that in human MAOB the loop from residue 99 to 112 separates the active site cavity from the solvent (*47*). In rat MAOA, the corresponding loop consists of residues 108−121. Mutational kinetic studies have shown that substitution of Gly110 with Ala decreases the enzyme's activity in solution 11-fold (*18*). Additionally, the entrance of the tunnel is in the proximity of the lipid membrane. Biogenic monoamines, which are hydrophobic and positively charged molecules, are expected to be concentrated at the lipid−water interface of the membrane. Therefore, we propose that this tunnel might be used for amine substrate uptake and aldehyde product release.

Along with the opening of the major tunnel, we observed the formation of a second minor tunnel, which leads in the opposite direction, passing by residues Ile180, Asn181, Val182, Thr183, Glu188, Gly301, Ala302, Val303, Leu354, Ala355, and Arg356 (Figure 9c). The average size of the minor tunnel was ~1 Å in the different runs, occasionally opening to ~1.5 Å (Table 2). Its size is sufficient for passage of small molecules, and indeed, the formation of a wire of water molecules could be observed in the runs.

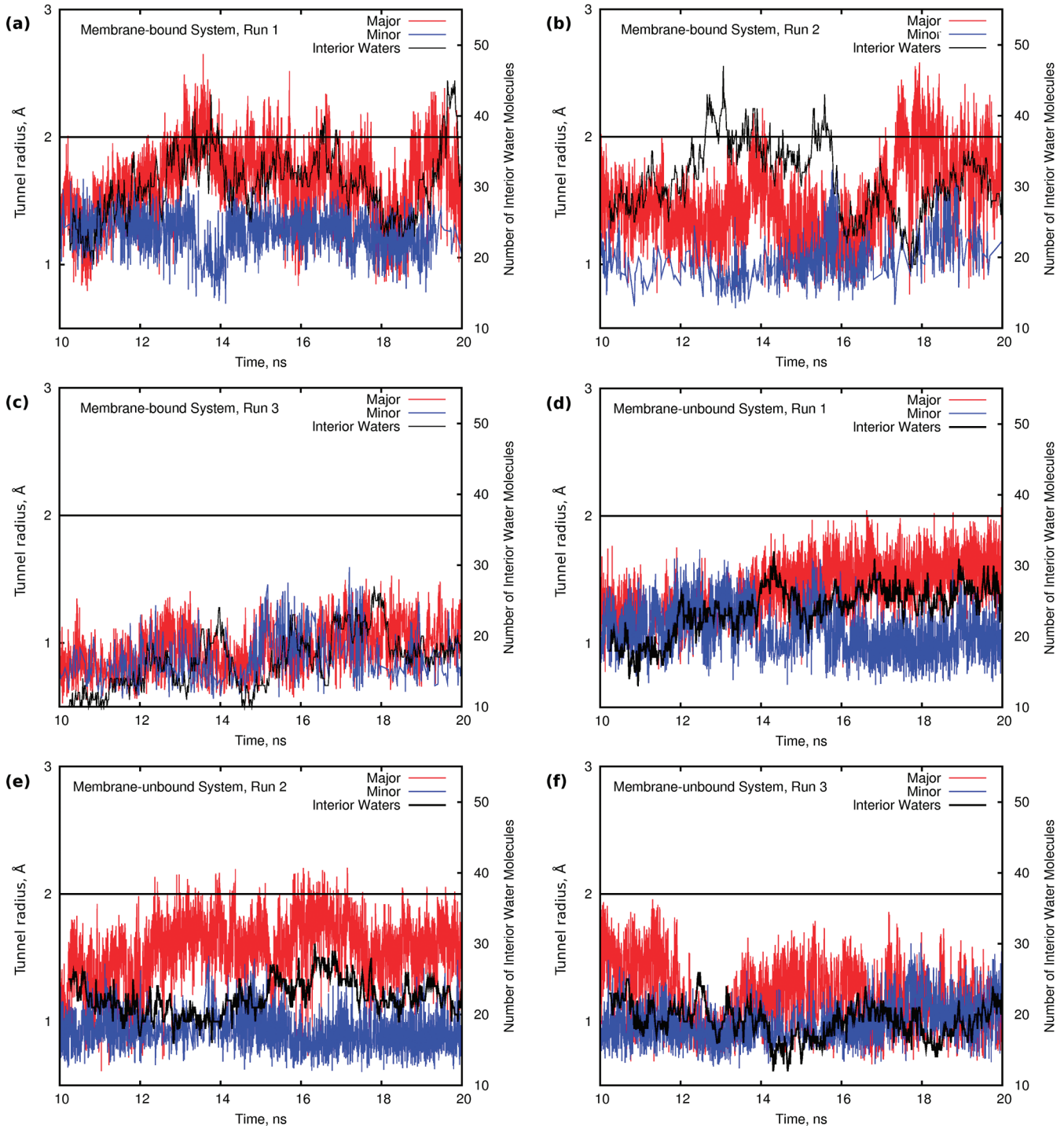

FIGURE 10: Radii of the tunnels and number of interior water molecules. The sizes of radii of the major (red lines) and minor (blue lines) tunnels are plotted using the left *y*-axis, while the number of interior water molecules (black lines) is plotted using the right *y*-axis of each panel. A tunnel radius size of 2 Å is shown for reference. In the first two of the membrane-bound system runs (a and b), the major tunnel opens above 2.5 Å which is sufficient for passage of a typical substrate (size of 2.25 Å). Moreover, there is a correlation in the major tunnel opening with an increase in the number of interior water molecules. In the third membrane-bound run (c), the MD simulation did not register a large conformational change. In all of the membrane-unbound system (d–f), the radii of the tunnels along with the number of interior water molecules remained rather constant, and no expansions were observed.

The wire was repeatedly interrupted, often coinciding with the opening event of the major tunnel. The oxidative deamination reaction that is catalyzed by MAOA ends with hydrogen peroxide and ammonia products. Access to bulk solvent along this tunnel from the reactive site near the substrate's amine group is shorter by 7 Å compared to that of the major tunnel. This minor tunnel might be used for the release of the ammonia and hydrogen peroxide products of the enzymatic deamination reaction.

In the membrane-unbound system, the average radii of the major and minor tunnels were comparable to those of the membrane-bound system ones (Figure 10d–f and Table 2) but never reached the high values observed in the membrane-bound system. Their sizes remained rather constant throughout the simulation, and no openings were observed. Although no water-filled pathways could be seen in the crystal structure of rat MAOA, we calculated the sizes of the two tunnels.

They were 1.18 and 0.73 Å for the major and minor one, respectively.

To confirm that the opening of the major tunnel in the membrane-bound system was accompanied by global structural modifications of the active site, rather than localized side chain rearrangements, we monitored the number of water molecules that occupy the interior of the active site and the two tunnels throughout the simulation trajectories. We extracted water molecules within 10 Å of the geometrical center of the residues lining the cavity. The cutoff was chosen to cover the whole active site volume without including bulk solvent. The results are shown in Figure 10 (black lines). They confirm that the observed openings of the major tunnel are accompanied by expansions of the active site, as seen from the increase in the number of water molecules in the protein interior. Correspondingly, such expansion did not occur in the membrane-unbound system. We did not observe expansion in one of the membrane-bound runs (Figure 10c), possibly due to insufficient sampling and time scale restrictions.

CONCLUSION

We have investigated the dynamical properties of rat MAOA and their dependence on the surrounding environment by performing 120 ns molecular dynamics simulations of the full-length monomer in a solvated POPC lipid bilayer, and of the truncated extracellular unit in water. Analysis of the correlations of the atomic fluctuations identified the existence of three dynamical domains within the extracellular unit.

In the membrane-bound system simulation, the movements of the membrane binding domain showed more pronounced anticorrelated motions with the substrate and FAD binding domains than in the membrane-unbound system. The reason for the decoupling of the domains is thought to be the steric restrictions imposed by the lipid bilayer on the embedded part of the protein, manifested in the dominant first-principal component mode of conformational change, as extracted using PCA analysis. A similar mode was found in the low-frequency spectrum of normal modes derived by ENM analysis, suggesting that inherent flexibility contained within the tertiary structure might be explored during the molecular dynamics run.

Fluctuations along the first-principal component mode in the membrane simulation are suggested to facilitate the observed expansion of the active site. The expansion was accompanied by the opening of a major tunnel of a size sufficient for passage of substrate molecules. The loops defining the gate of the tunnel contain the conserved Gly110 and Phe208 residues. The importance of these residues for enzyme function has been confirmed by mutational analysis. A second tunnel was found to lead in the opposite direction of the entrance tunnel. Its size, permissible for passage of products of the enzymatic reaction, and the proximity of the reaction center make it a convenient route for product removal. Further experimental validation is required for the role of this minor tunnel. Analysis of the membrane-unbound system simulation trajectories did not indicate significant enlargement of either of the tunnels. We also did not observe expansion of the active site to the extent seen in the membrane-bound system. This result can be attributed to the stronger coupling between the membrane domain and the rest of the truncated unit.

Kinetic analysis studies of MAO homologues have shown that truncation of the TM helix and the outer loop leads to enzyme instability and a 10-fold drop in activity (*20*). It has also been suggested (*47*, *42*) that membrane anchoring positions MAOs near the substrate source. Our findings propose the mechanism through which the membrane environment facilitates enzymatic function, namely, decoupling of interdomain motions within the extracellular unit upon membrane insertion by constraining the movements of helix TM and membrane binding domain M. Membrane-associated outer loop L restricts and guides the dynamics of the S and F domains, resulting in complex twist- and closure-like motions that expand the active site cavity and open a route for substrate access, as seen from the dominant first-principal component of the membrane-embedded system.

ACKNOWLEDGMENT

We thank Prof. Tomitake Tsukihara and Dr. Seyoung Son at the Institute for Protein Research, Osaka University, for valuable discussions and comments. We also thank Dr. Narutoshi Kamiya at the Center for Advanced Medical Engineering and Informatics, Osaka University, for helpful discussions.

REFERENCES

(1) Youdim, M. B. H., Edmondson, D., and Tipton, K. F. (2006) The therapeutic potential of monoamine oxidase inhibitors. *Nat. Rev. Neurosci. 7*, 295–309.
(2) Shih, J. C., Chen, K., and Ridd, M. J. (1999) Monoamine oxidase: From genes to behavior. *Annu. Rev. Neurosci. 22*, 197–217.
(3) Gareri, P., Falconi, U., Fazio, P. D., and Sarro, G. D. (2000) Conventional and new antidepressant drugs in the elderly. *Prog. Neurobiol. 61*, 353–396.
(4) Pletscher, A. (1991) The discovery of antidepressants: A winding path. *Experientia 47*, 4–8.
(5) Grimsby, J., Toth, M., Chen, K., Kumazawa, T., Klaidman, L., Adams, J. D., Karoum, F., Gal, J., and Shih, J. C. (1997) Increased stress response and β-phenylethylamine in MAOB-deficient mice. *Nat. Genet. 17*, 206–210.
(6) Yu, P. H., Davis, B. A., and Boulton, A. A. (1995) Aliphatic propargylamines, a new series of potent selective, irreversible non-amphetamine-like MAO-B inhibitors. Their structures, function and pharmacological implications. *Adv. Exp. Med. Biol. 363*, 17–23.
(7) Qin, F., Shite, J., Mao, W., and Seng Liang, C. (2003) Selegiline attenuates cardiac oxidative stress and apoptosis in heart failure: Association with improvement of cardiac function. *Eur. J. Pharmacol. 461*, 149–158.
(8) Simon, L., Szilagyi, G., Bori, Z., Orbay, P., and Nagy, Z. (2001) (−)-D-Deprenyl attenuates apoptosis in experimental brain ischaemia *Eur. J. Pharmacol. 430*, 235–241.
(9) Youdim, M. B., and Weinstock, M. (2001) Molecular basis of neuroprotective activities of rasagiline and the anti-alzheimer drug tv3326 [(n-propargyl-(3r)aminoindan-5-yl)-ethyl methyl carbamate]. *Cell. Mol. Neurobiol. 21*, 555–573.
(10) Patel, S. V., Tariot, P. N., and Asnis, J. (1996) L-Deprenyl augmentation of fluoxetine in a patient with Huntington's disease. *Ann. Clin. Psychiatry 8*, 23–26.
(11) Waibel, S., Reuter, A., Malessa, S., Blaugrund, E., and Ludolph, A. C. (2004) Rasagiline alone and in combination with riluzole prolongs survival in an ALS mouse model. *J. Neurol. 251*, 1080–1084.
(12) Chimenti, F., Maccioni, E., Secci, D., Bolasco, A., Chimenti, P., Granese, A., Befani, O., Turini, P., Alcaro, S., Ortuso, F., Cardia, M. C., and Distinto, S. (2007) Selective inhibitory activity against MAO and molecular modeling studies of 2-thiazolylhydrazone derivatives. *J. Med. Chem. 50*, 707–712.
(13) Harkcom, W. T., and Bevan, D. R. (2007) Molecular docking of inhibitors into monoamine oxidase B. *Biochem. Biophys. Res. Commun. 360*, 401–406.
(14) Toprakci, M., and Yelekci, K. (2005) Docking studies on monoamine oxidase-B inhibitors: Estimation of inhibition constants (k_i) of a series of experimentally tested compounds. *Bioorg. Med. Chem. Lett. 15*, 4438–4446.
(15) Yelekci, K., Karahan, O., and Toprakci, M. (2007) Docking of novel reversible monoamine oxidase-B inhibitors: Efficient prediction of ligand binding sites and estimation of inhibitors thermodynamic properties. *J. Neural Transm. 114*, 725–732.

(16) Colibus, L. D., Li, M., Binda, C., Lustig, A., Edmondson, D. E., and Mattevi, A. (2005) Three-dimensional structure of human monoamine oxidase A (MAO A): Relation to the structures of rat MAO A and human MAO B. *Proc. Natl. Acad. Sci. U.S.A. 102*, 12684–12689.
(17) Ma, J., Yoshimura, M., Yamashita, E., Nakagawa, A., Ito, A., and Tsukihara, T. (2004) Structure of rat monoamine oxidase A and its specific recognitions for substrates and inhibitors. *J. Mol. Biol. 338*, 103–114.
(18) Son, S.-Y., Ma, J., Kondou, Y., Yoshimura, M., Yamashita, E., and Tsukihara, T. (2008) Structure of human monoamine oxidase A at 2.2-Å resolution: The control of opening the entry for substrates/inhibitors. *Proc. Natl. Acad. Sci. U.S.A. 105*, 5739–5744.
(19) Cruz, F., and Edmondson, D. E. (2007) Kinetic properties of recombinant MAO-A on incorporation into phospholipid nanodisks. *J. Neural Transm. 114*, 699–702.
(20) Rebrin, I., Geha, R. M., Chen, K., and Shih, J. C. (2001) Effects of carboxyl-terminal truncations on the activity and solubility of human monoamine oxidase B. *J. Biol. Chem. 276*, 29499–29506.
(21) Karplus, M., and McCammon, J. A. (2002) Molecular dynamics simulations of biomolecules. *Nat. Struct. Biol. 9*, 646–652.
(22) Suhre, K., and Sanejouand, Y.-H. (2004) Elnemo: A normal mode web server for protein movement analysis and the generation of templates for molecular replacement. *Nucleic Acids Res. 32*, W610–W614.
(23) Tirion (1996) Large amplitude elastic motions in proteins from a single-parameter, atomic analysis. *Phys. Rev. Lett. 77*, 1905–1908.
(24) Fukunishi, Y., Mikami, Y., and Nakamura, H. (2003) The filling potential method: A method for estimating the free energy surface for protein-ligand docking. *J. Phys. Chem. B 107*, 13201–13210.
(25) Frisch, M. J., Trucks, G. W., Schlegel, H. B., Scuseria, G. E., Robb, M. A., Cheeseman, J. R., Montgomery, J. A., Jr., Vreven, T., Kudin, K. N., Burant, J. C., Millam, J. M., Iyengar, S. S., Tomasi, J., Barone, V., Mennucci, B., Cossi, M., Scalmani, G., Rega, N., Petersson, G. A., Nakatsuji, H., Hada, M., Ehara, M., Toyota, K., Fukuda, R., Hasegawa, J., Ishida, M., Nakajima, T., Honda, Y., Kitao, O., Nakai, H., Klene, M., Li, X., Knox, J. E., Hratchian, H. P., Cross, J. B., Bakken, V., Adamo, C., Jaramillo, J., Gomperts, R., Stratmann, R. E., Yazyev, O., Austin, A. J., Cammi, R., Pomelli, C., Ochterski, J. W., Ayala, P. Y., Morokuma, K., Voth, G. A., Salvador, P., Dannenberg, J. J., Zakrzewski, V. G., Dapprich, S., Daniels, A. D., Strain, M. C., Farkas, O., Malick, D. K., Rabuck, A. D., Raghavachari, K., Foresman, J. B., Ortiz, J. V., Cui, Q., Baboul, A. G., Clifford, S., Cioslowski, J., Stefanov, B. B., Liu, G., Liashenko, A., Piskorz, P., Komaromi, I., Martin, R. L., Fox, D. J., Keith, T., Al-Laham, M. A., Peng, C. Y., Nanayakkara, A., Challacombe, M., Gill, P. M. W., Johnson, B., Chen, W., Wong, M. W., Gonzalez, C., and Pople, J. A. (2004) Gaussian 03 , revision c.02, Gaussian, Inc., Wallingford, CT.
(26) Shiloff, B. A., Behrens, P. Q., Kwan, S. W., Lee, J. H., and Abell, C. W. (1996) Monoamine oxidase B isolated from bovine liver exists as large oligomeric complexes in vitro. *Eur. J. Biochem. 242*, 41–50.
(27) MacKerell, A., Bashford, D., Bellott, M., Dunbrack, R., Evanseck, J., Field, M., Fischer, S., Gao, J., Guo, H., Ha, S., Joseph-McCarthy, D., Kuchnir, L., Kuczera, K., Lau, F., Mattos, C., Michnick, S., Ngo, T., Nguyen, D., Prodhom, B., Reiher, W., Roux, B., Schlenkrich, M., Smith, J., Stote, R., Straub, J., Watanabe, M., Wiorkiewicz-Kuczera, J., Yin, D., and Karplus, M. (1998) All-atom empirical potential for molecular modeling and dynamics studies of proteins. *J. Phys. Chem. B 102*, 3586–3616.
(28) Terada, T., and Kidera, A. (2002) Generalized form of the conserved quantity in constant-temperature molecular dynamics. *J. Chem. Phys. 116*, 33–41.
(29) Essmann, U., Perera, L., Berkowitz, M. L., Darden, T., Lee, H., and Pedersen, L. G. (1995) A smooth particle mesh ewald method. *J. Chem. Phys. 103*, 8577–8593.
(30) Narumi, T., Ohno, Y., Futatsugi, N., Okimoto, N., Suenaga, A., Yanai, R., and Taiji, M. (2006) A High-Speed Special-Purpose Computer for Molecular Dynamics Simulations: MDGRAPE-3 , NIC Series, Vol. 34, pp 29−35.
(31) Amadei, A., Linssen, A. B., and Berendsen, H. J. (1993) Essential dynamics of proteins. *Proteins 17*, 412–425.
(32) Kitao, A., and Go, N. (1999) Investigating protein dynamics in collective coordinate space. *Curr. Opin. Struct. Biol. 9*, 164–169.
(33) Hayward, S., and Berendsen, H. J. (1998) Systematic analysis of domain motions in proteins from conformational change: New results on citrate synthase and t4 lysozyme. *Proteins 30*, 144–154.
(34) Alexandrov, N., and Shindyalov, I. (2003) PDP: Protein domain parser. *Bioinformatics 19*, 429–430.
(35) Petrek, M., Otyepka, M., Bans, P., Kosinov, P., Koca, J., and Damborsk, J. (2006) Caver: A new tool to explore routes from protein clefts, pockets and cavities. *BMC Bioinf. 7*, 316.
(36) Humphrey, W., Dalke, A., and Schulten, K. (1996) VMD: Visual molecular dynamics. *J. Mol. Graphics 14*, 33–38.
(37) Thompson, J. D., Higgins, D. G., and Gibson, T. J. (1994) CLUSTAL W: Improving the sensitivity of progressive multiple sequence alignment through sequence weighting, position-specific gap penalties and weight matrix choice. *Nucleic Acids Res. 22*, 4673–4680.
(38) Galtier, N., Gouy, M., and Gautier, C. (1996) SEAVIEW and PHYLO_WIN two graphic tools for sequence alignment and molecular phylogeny. *Comput. Appl. Biosci. 12*, 543–548.
(39) Gnuplot (2007) http://www.gnuplot.info.
(40) Lyx (2007) http:///www.lyx.org.
(41) Jabref (2007) http://www.jabref.sourceforge.net/.
(42) Fowler, P. W., Balali-Mood, K., Deol, S., Coveney, P. V., and Sansom, M. S. P. (2007) Monotopic enzymes and lipid bilayers: A comparative study. *Biochemistry 46*, 3108–3115.
(43) Tsugeno, Y., and Ito, A. (1997) A key amino acid responsible for substrate selectivity of monoamine oxidase A and B. *J. Biol. Chem. 272*, 14033–14036.
(44) Ma, J. (2005) Usefulness and limitations of normal mode analysis in modeling dynamics of biomolecular complexes. *Structure 13*, 373–380.
(45) Cui, Q., Li, G., Ma, J., and Karplus, M. (2004) A normal mode analysis of structural plasticity in the biomolecular motor F_1-ATPase. *J. Mol. Biol. 340*, 345–372.
(46) Lu, M., and Ma, J. (2005) The role of shape in determining molecular motions. *Biophys. J. 89*, 2395–2401.
(47) Binda, C., Newton-Vinson, P., Hubalek, F., Edmondson, D. E., and Mattevi, A. (2002) Structure of human monoamine oxidase B, a drug target for the treatment of neurological disorders. *Nat. Struct. Biol. 9*, 22–26.